Zhang, Y., Wang, R., Chen, Y.-T. (2015): Stability of rapid finite-fault inversion for the 2014 Mw 6.1 South Napa earthquake. - *Geophysical Research Letters*, *42*, 23, pp. 10,263—10,272.

DOI: http://doi.org/10.1002/2015GL066244

AGU PUBLICATIONS

Geophysical Research Letters

RESEARCH LETTER
10.1002/2015GL066244

Key Points:
- Different network stations result in similar rupture direction and major slip area
- Errors in hypocenter and fault geometry do not significantly change the rupture images
- The rupture processes can be imaged in real time with real strong motion seismograms

Supporting Information:
- Figures S1–S11

Correspondence to:
Y. Zhang,
zhygn@163.com

Citation:
Zhang, Y., R. Wang, and Y.-T. Chen (2015), Stability of rapid finite-fault inversion for the 2014 M_w6.1 South Napa earthquake, *Geophys. Res. Lett.*, *42*, 10,263–10,272, doi:10.1002/2015GL066244.

Received 18 SEP 2015
Accepted 19 NOV 2015
Accepted article online 23 NOV 2015
Published online 11 DEC 2015

Stability of rapid finite-fault inversion for the 2014 M_w6.1 South Napa earthquake

Yong Zhang[1], Rongjiang Wang[2], and Yun-Tai Chen[1,3]

[1]School of Earth and Space Sciences, Peking University, Beijing, China, [2]Helmholtz Centre Potsdam GFZ German Research Centre for Geosciences, Potsdam, Germany, [3]Institude of Geophysics, China Earthquake Administration, Beijing, China

Abstract Local seismograms are useful for rapidly reconstructing kinematic finite-fault sources, but the results often depend not only on the data coverage but also on uncertainties of parameters (e.g., hypocentral location and fault geometry) used as a priori information during the inversion. An automatic scheme was applied to offline tests for the 2014 South Napa earthquake. In the case of retrospective full-waveform inversions, a network with station spacing of 10 km within the epicentral distance of 30 km is able to provide adequate stable key source parameters if the preestimated hypocenter and fault orientation are accurate of ±5 km and ±15°, respectively. In simulated real-time inversions, the magnitude reaches M_w6.0 at 13 s, and the slip distribution matches that from the retrospective inversion at about 22–28 s after the origin time of the earthquake. These results are meaningful for estimating the lead time of a catastrophic seismic event.

1. Introduction

To effectively estimate the earthquake disasters, it is important and necessary to determine the source parameters, which contain the hypocentral location, source mechanism (fault geometry), slip distribution, and kinematic rupture processes. So far, both the hypocentral locations and source mechanisms of earthquakes can be estimated automatically and routinely [e.g., *Hayes et al*., 2009]. Some studies have shown that the mechanism and fault geometry can be deduced very quickly if the near-field seismogeodetic data are available [e.g., *Melgar et al*., 2012; *Minson et al*., 2014; *J. Zhang et al*., 2014]. Moreover, estimating the slip model with the elastic dislocation theory [*Okada*, 1985; *Wang et al*., 2006] has become an important part of the GPS seismology. By inverting coseismic displacements of geodetic high-rate GPS data, a series of source parameters, such as the moment magnitude, fault geometry, fault dimension, and static slip distribution, can be estimated in real time or near real time [*Crowell et al*., 2009; *Falck et al*., 2010; *Allen and Ziv*, 2011; *Wright et al*., 2012; *Colombelli et al*., 2013; *Li et al*., 2013; *Hoechner et al*., 2013; *Grapenthin et al*., 2014; *Gusman et al*., 2014; *Minson et al*., 2014]. These source parameters are valuable to earthquake emergency responses (EERs) and earthquake early warnings (EEWs). Compared with waveform inversions, geodetic estimates need not to solve for rupture times or rupture velocities, leading to a stronger stability and higher efficiency than the waveform inversions. On the other hand, however, no or worse time resolution of the geodetic inversions may lead to an underestimate of the disasters by ignoring the directivity effect of seismic waves.

Since the 1980s, seismologists have invested large efforts to develop various methods for estimating the spatiotemporal rupture processes of earthquakes [*Olson and Apsel*, 1982; *Kikuchi and Kanamori*, 1982; *Hartzell and Heaton*, 1983; *Mori and Hartzell*, 1990; *Das and Kostrov*, 1994; *Chen and Xu*, 2000; *Ji et al*., 2002; *Vallée*, 2004; *Yagi et al*., 2004; *Monelli and Mai*, 2008; *Zhang et al*., 2012]. The major target of these studies was to better understand the physics of earthquakes. Methods for this purpose were mainly manually operated with some empirical preassumed limitations. Therefore, they are less applicable to EER and EEW, though it has been widely recognized that a detailed source rupture model is relevant for that [e.g., *Allen et al*., 2009]. Especially in the last few decades, the occurrence of large disastrous earthquakes with dimensions spanning hundreds of kilometers further highlighted this demand. So that the rupture model can be applied to EER and EEW, it must be determined robustly, efficiently, and automatically. Some efforts have been made on this aspect. *Dreger and Kaverina* [2000] developed a method to estimate the finite source and simulate strong ground motions. This method was then automated and successfully applied to the 2003 M_w6.5 San Simeon and 2004 M_w6.0 Parkfield earthquakes [*Dreger et al*., 2005]. Due to the automation of the method, the rupture model could be estimated within 30 min after the earthquake occurrence. Recently, *Y. Zhang et al*. [2014] developed an iterative deconvolution and stacking (IDS) method for automatic

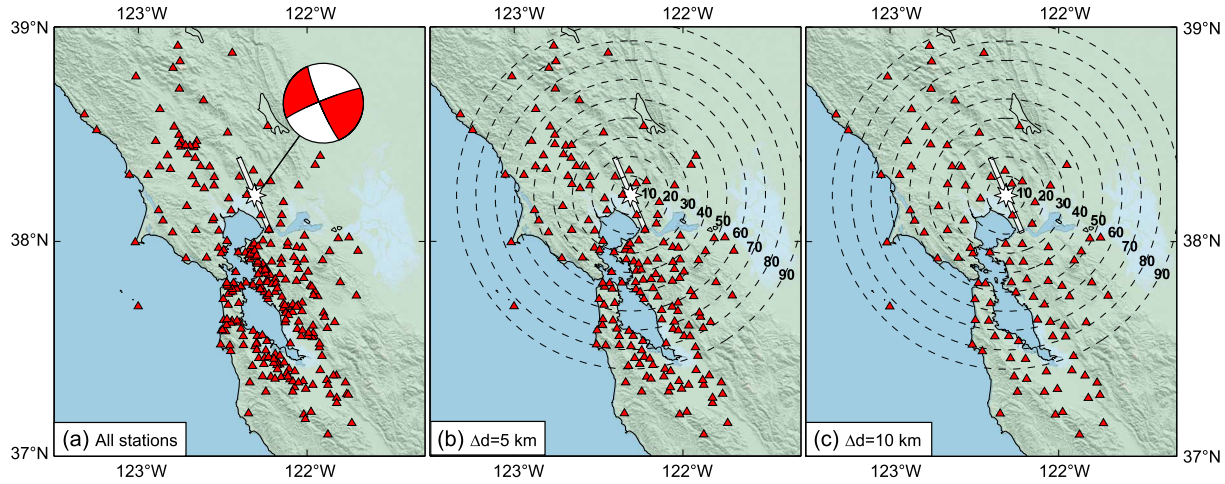

Figure 1. Map view of the epicentral area of the 2014 South Napa earthquake. White star denotes the epicenter located by USGS. The white rectangle and red triangles represent the surface projection of the fault plane and the strong motion stations, respectively. (a) All strong motion stations and the GCMT focal solution (beach ball). (b) Stations reselected with spacing of 5 km. (c) Stations reselected with spacing of 10 km.

imaging of rupture process, in which there is no need to solve linear or nonlinear equations. The robustness and efficiency of the IDS method have been demonstrated in applications to the 2008 Wenchuan and 2011 Tohoku earthquakes [*Y. Zhang et al.*, 2014], which help to reduce the response time as much as possible.

Though there have been successful tests for real-time or near-real-time kinematic inversions, some practical problems still exist. During an earthquake emergency, however, data are generally not abundant and tend to be unevenly distributed, and the fast determined hypocenter and fault geometry may have some uncertainties or errors, all of which may cause unpredictable instabilities of finite-fault inversions. Before a rupture model can be applied to EER and EEW, the extent of these instabilities has to be investigated.

The 24 August 2014 South Napa M_w6.1 earthquake occurred about 9 km south-southwest of Napa at 10:20:44 (UTC). It was the largest event in the San Francisco Bay Area, California, since the 1989 Loma Prieta M_w6.9 quake [*Wald et al.*, 1991]. California has long been seismically active, with the famous San Andreas Fault delineating the boundary between the Pacific and North American Plates, resulting in many strong and large earthquakes. With a strong demand of disaster mitigation, some studies have focused on the realization of EEW in the California area [*Kanamori et al.*, 1997; *Allen and Kanamori*, 2003; *Wurman et al.*, 2007; *Cua et al.*, 2009].

The South Napa earthquake was well recorded by a dense strong motion network. With the strong motion waveform data, we carried out a series of tests of kinematic source inversions using the IDS method. The purpose was to assess the stabilities of automatic rupture process inversions, i.e., how much the rupture model would change with different network configurations, and uncertainties of the hypocenter location and fault geometry. Additionally, we also simulated real-time analyses by inverting incomplete strong motion seismograms to evaluate how fast the ruptures could be stably imaged after their occurrences.

2. Data Processing and Source Parameters

The strong motion data used in the present study are provided by the Center for Engineering Strong Motion Data (CESMD). The raw acceleration seismograms (with baselines uncorrected) were integrated twice into displacement seismograms and then were filtered using a band-pass filter of 0.02–0.5 Hz. All stations with three-component waveforms were considered (Figure 1a). To well simulate a rapid response to an earthquake, we did not check the quality of the data but weighted all waveform components equally in inversions.

The hypocenter of the South Napa earthquake was located at 38.215°N, 122.312°W and depth of 11.3 km by the United States Geological Survey (USGS). The mechanisms released by different earthquake agencies are in good agreement, all of which suggest a right-lateral strike-slip fault along the SSE-NNW direction. In this study, we choose fault geometry of the Global Centroid Moment Tensor (GCMT) solution, that is, strike = 157°,

dip = 83°, and rake = 174°. In the latter part of this paper, we will test and discuss the probable uncertainties of the hypocentral location and fault geometry.

Soon after the earthquake, there exists generally no prior knowledge related to the rupture direction or dimension. Therefore, the finite-fault plane should be large enough to recover any potential rupture propagations. In the present case, a 42 km long and 20 km wide fault plane is used, which is then equally divided into 21 and 10 subfaults along the strike and downdip directions, respectively. According to the USGS solution, the hypocenter (rupture initiation point) was placed at the eleventh and sixth subfaults. In inversions using the IDS method, the maximum rupture velocity is commonly fixed at 6 km/s (approximate velocity of *P* waves in the upper crust), and the rupture duration of each subfault is unrestricted. The waveform Green's functions were calculated using the code "Qseis" [*Wang*, 1999] based on the GIL7 curst model [*Stidham et al*., 1999].

3. Tests of Different Network Configurations

The quality or reliability of rupture models are well known to closely depend on the network coverage. Some researchers have conducted tests to assess what network is adequate to constrain a rupture model [*Miyatake et al*., 1986; *Olson and Anderson*, 1988; *Iida et al*., 1990; *Sarao et al*., 1998; *Beresnev*, 2003; *Zhou et al*., 2004; *Asano and Iwata*, 2009; *Zhang et al*., 2015]. These studies have drawn some quasi-quantitative conclusions, which are useful in evaluating rupture models. However, some differences exist among the conclusions of these researchers. For example, *Sarao et al*. [1998] found that four stations in the rupture direction were sufficient to deduce the rupture images, *Asano and Iwata* [2009] concluded that 12 stations are generally needed for a stable inversion, and *Zhang et al*. [2015] pointed out that a single station was basically feasible to support the production of an acceptable rupture model. These different evaluations are attributed to the various inversion methods with different empirical constraints [*Beresnev*, 2003].

With the automatic IDS method, the subjective influence can be largely minimized. In addition, we use the real recordings rather than synthetic data to consider complex errors in both observations and Earth structures, creating a situation more close to reality. Meanwhile, the weakness is that the network stations cannot be varied arbitrarily.

Based on the dense strong motion stations (Figure 1a), we reconstructed networks with different epicentral distances (R) and station spacings (Δd). The epicentral distances range from 10 km to more than 90 km in 10 km step. Two station spacings (5 km and 10 km) were considered independently (Figures 1b and 1c). Totally, we have 20 network configurations for the tests. Figures 2a and 2b show slip models obtained from these 20 networks. Overall, all slip models are consistent with each other in their major characteristics. The most significant slip patch is located to the upper left of the hypocenter, which means that the rupture mainly propagated to the north and at the shallow depth. This is consistent with other seismic and geodetic studies [*Barnhart et al*., 2015; *Dreger et al*., 2015; *Feng et al*., 2015; *Ji et al*., 2015; *Melgar et al*., 2015; *Wei et al*., 2015]. Most slip distributions shown in Figures 2a and 2b seem relatively tight and smoothed, which are close to joint and geodetic GPS/interferometric synthetic aperture radar models [*Barnhart et al*., 2015; *Dreger et al*., 2015; *Feng et al*., 2015; *Melgar et al*., 2015], but differ with results of velocity waveform inversions of strong motion data [*Ji et al*., 2015; *Wei et al*., 2015]. The reason may be that we inverted displacement waves, in which waveform information at low frequencies has larger weight than that at high frequencies.

Subfault source time functions (STFs) were also well retrieved in most cases (Figures S1 and S2 in the supporting information). By considering the centroid time of subfault STFs, we calculated the slip-weighted average rupture velocities for each rupture model. They are between 2.7 and 3.1 km/s, close to 2.9–3.0 km/s obtained by other waveform inversions [*Dreger et al*., 2015; *Ji et al*., 2015; *Melgar et al*., 2015; *Wei et al*., 2015]. In inversions of $R > 10$ km, subfault STFs show similar rupture times and durations but different amplitudes (moment rate). For $R \leq 10$ km, however, since only one or two stations were used, subfault STFs show unreasonable complex time histories. It suggests that with the use of very few stations, the slip patch could be stably imaged [*Zhang et al*., 2015], but the subfault STFs are less constrained.

We found some interesting differences associated with the networks (Figures 2c–2e). For four inversions of $R \leq 20$ km, the magnitudes are slightly overestimated (~M_w6.2–6.4), which resulted probably from overfitting

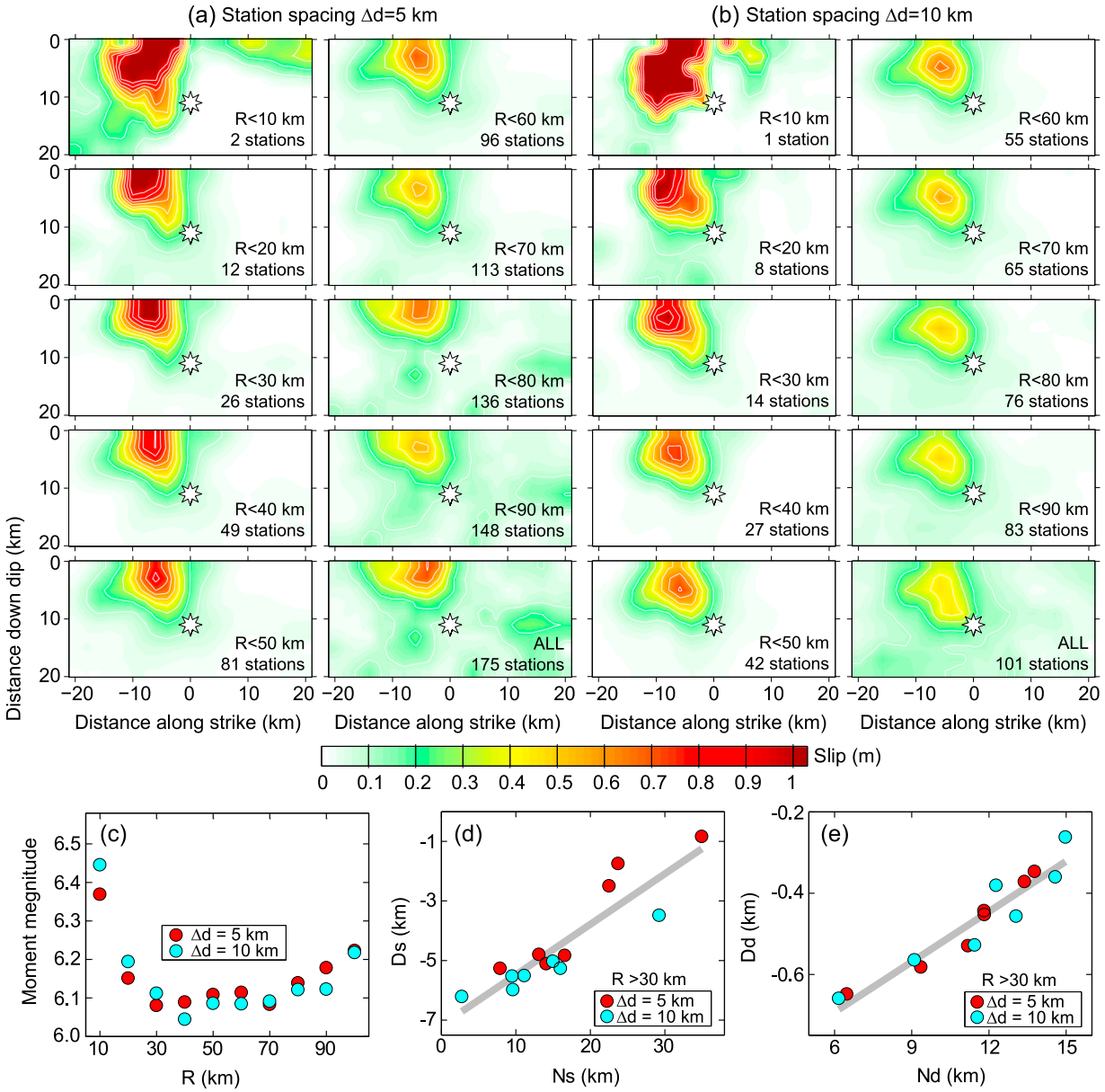

Figure 2. Automatic finite-fault source models obtained using different network configurations. (a) Slip distributions depending on networks with different distance coverages and an approximately uniform spacing of 5 km. (b) Same as Figure 2a but for station spacing of 10 km. (c) Comparison of moment magnitudes for the slip models shown in Figures 2a and 2b. (d) Comparison of the slip centroid locations (Ds) in dependence of the network centroid locations (Ns) relative to the epicenter in the strike (157°) direction, where the solid line shows the linear regression between them. (e) Same as Figure 2d but for comparison of the two centroid locations (Dd and Nd) in the dip (247°) direction.

of very few waveforms. When R is between 30 km and 70 km, the magnitudes stably range from M_w6.04 to M_w6.11. When $R > 70$ km, some scattered slips appear at depth. Because of the increasing shear modulus with depth, the deep slip noises have a considerable contribution to the seismic moment, causing the gradual magnitude increase to M_w6.2 (Figure 2c).

As R increases, the stations to the south and west of the epicenter become more predominant, which are probably related to the deep slips appeared at $R > 70$ km. *Olson and Anderson* [1988] and *Hartzell et al.* [2007] have pointed out that slips tend to be distributed at the predominant direction of station azimuths. Using the results shown in Figures 2a and 2b, we checked the statistic relationship between the fault slips and networks used. For each slip model, we calculated the centroids of both slips and network coordinates

and compared their distances from the epicenter in strike and dip directions, respectively (Figures 2d and 2e). We found that they are linearly related. This finding clearly confirms that slips tend to be located toward the seismic stations. Our explanation of the phenomenon is the following: It is known that the inversions are generally realized by minimizing the residuals between the synthetics and observations of the L1 or L2 norm. To increase the solution stability, the minimum energy constraint is normally used explicitly or implicitly. The retrieved ruptures would be closer to stations than their real positions when they equally fit the data. Accordingly, the peak slips will be somewhat underestimated. This problem has also been encountered in geodetic analysis of the 2011 Tohoku M_w9.0 earthquake [*Pollitz et al*., 2011]. From inland GPS data estimates, the slips are always closer to the coast, resulting in peak slips of about 30 m, less than 50–60 m from inversions with seafloor GPS offsets [*Pollitz et al*., 2011; *Wang et al*., 2013].

It is also noticed that there are some shallow slip deficits in rupture models of $\Delta d = 10$ km compared with those of $\Delta d = 5$ km. This may be caused by the ratio between near-fault and off-fault stations. From inversion tests with networks at different distances (see Figure S3), near-fault stations lead to more significant shallow slips than distant stations. Three factors may have caused these differences. The first one is the inaccuracy of fault position, which could be caused by errors in hypocentral location and fault geometry, and fault irregularities. It leads to relatively large errors in near-fault inversions. At distant stations, this inaccuracy becomes little. The second factor is the 3-D heterogeneity and anisotropy of Earth structure, which can result in complex differences. The third factor, as we have discussed in the upper paragraph, is the uneven station distributions causing less shallow slips in the distant network inversions. Because of these reasons, it is hard to accurately determine the real value of shallow slips through inversions. Actually, the differences in shallow slips among the published slip models are commonly significant [*Barnhart et al*., 2015; *Dreger et al*., 2015; *Feng et al*., 2015; *Ji et al*., 2015; *Melgar et al*., 2015; *Wei et al*., 2015].

Overall, the inversion results show common source characteristics even with networks having different epicentral distances and station spacings (Figure 2). To produce a rapid response, they are all basically acceptable since both the northward rupture propagations and shallow ruptures were well imaged. Meanwhile, some differences also exist among these models in magnitude, slip distribution, and peak slips, which are mainly associated with the station distributions. By considering both uniform azimuthal coverage and number of stations, rupture models estimated from networks having epicentral distances 30–70 km and station spacing 10 km are preferred. This means that the minimum epicentral distance (30 km) is approximately 2 times the rupture dimension. In addition, the minimum number of stations is 14 ($R < 30$ km, $\Delta d = 10$ km). This closely agrees with the conclusion of *Asano and Iwata* [2009], who found that 12 stations are suitable for a stable inversion.

4. Errors of Hypocentral Location and Fault Geometry

Hypocentral location and fault geometry are basic source parameters needed in the kinematic source inversion. When performing automatic source imaging, the fast determined hypocenter and mechanism may have relatively large errors. Accordingly, the influences of their uncertainties should be investigated.

We assumed that errors of hypocentral location in the horizontal and vertical directions are both 5 km, which is comparable to the average station spacing of the strong motion network. According to *Helffrich* [1997], we used errors of fault geometry of 15°. For each given hypocenter, we chose stations within the epicentral distances of 30 km and reselected them with a spacing of 10 km for the inversions (Figure 3).

To consider the effects of hypocenter uncertainty along the dip direction, we changed the epicenter ±5 km perpendicular to the fault strike. For the geometry uncertainty, we altered the fault strike, dip, and rake by ±15°. Totally, 16 combinations of the four parameters exist with the maximum and minimum values. In each case of inversion, we assume that the rupture initiates within an area instead of at a point to consider the hypocenter uncertainty along the strike and downdip directions. The radius of the area is equivalent to the hypocenter uncertainty (i.e., 5 km). Within the area, rupture velocity was unlimited and could be infinite (see Figure S4).

Figure 3 shows the surface projections of the fault slips obtained through the 16 inversions. Although various epicenters and fault geometries were used, the major rupture characteristics were still stably estimated. The 16 rupture models consistently show unilateral ruptures propagating to the north-northwest and at shallow

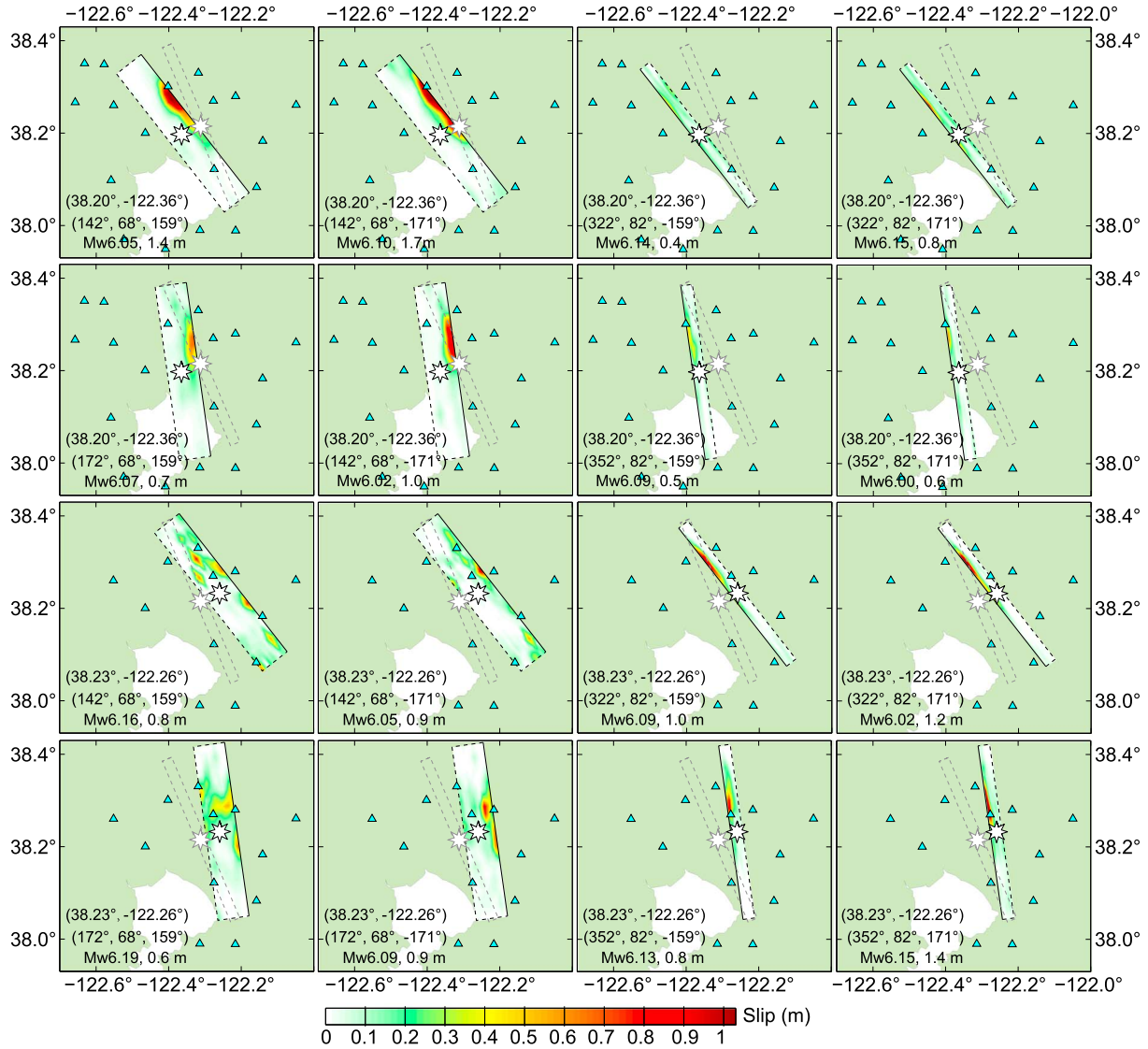

Figure 3. Surface projections of fault slips obtained using disturbed hypocenter locations (dark stars) and fault geometries (dark rectangles). For comparison the officially released epicenter and fault geometry are shown by the light star and rectangle, respectively. Text on the bottom left label detailed the epicenter and fault geometry used and the moment magnitude and peak slip obtained. Triangles are the strong motion stations ($R < 30$ km, $\Delta d = 10$ km) used.

depths. The moment magnitudes are between M_w6.00 and M_w6.19, i.e., with an average of M_w6.10 and uncertainty of ±0.1. The peak slip varies from 0.4 m to 1.7 m, suggesting a higher uncertainty than the magnitude estimates. Note that this uncertainty is comparable with the published slip models of the earthquake, in which peak slips were found between 0.8 m and 2.4 m [*Barnhart et al.*, 2015; *Dreger et al.*, 2015; *Ji et al.*, 2015; *Melgar et al.*, 2015; *Wei et al.*, 2015].

5. Real-Time Analysis

Real-time analysis of the waveform data is important because it produces the earliest estimates of the rupture source. For above 16 cases (Figure 3), in which uncertainties of the hypocentral location and fault geometry have been considered, we analyzed the strong motion data in real time by inverting incomplete seismograms at different time as they became available. The results would reveal "what can be seen" from the recordings, while the postanalysis gives "what has occurred" at the source. From Figure 4a, the time delay between the magnitudes of real-time analysis and postanalysis is 5–7 s, which is mainly associated with the traveltime of

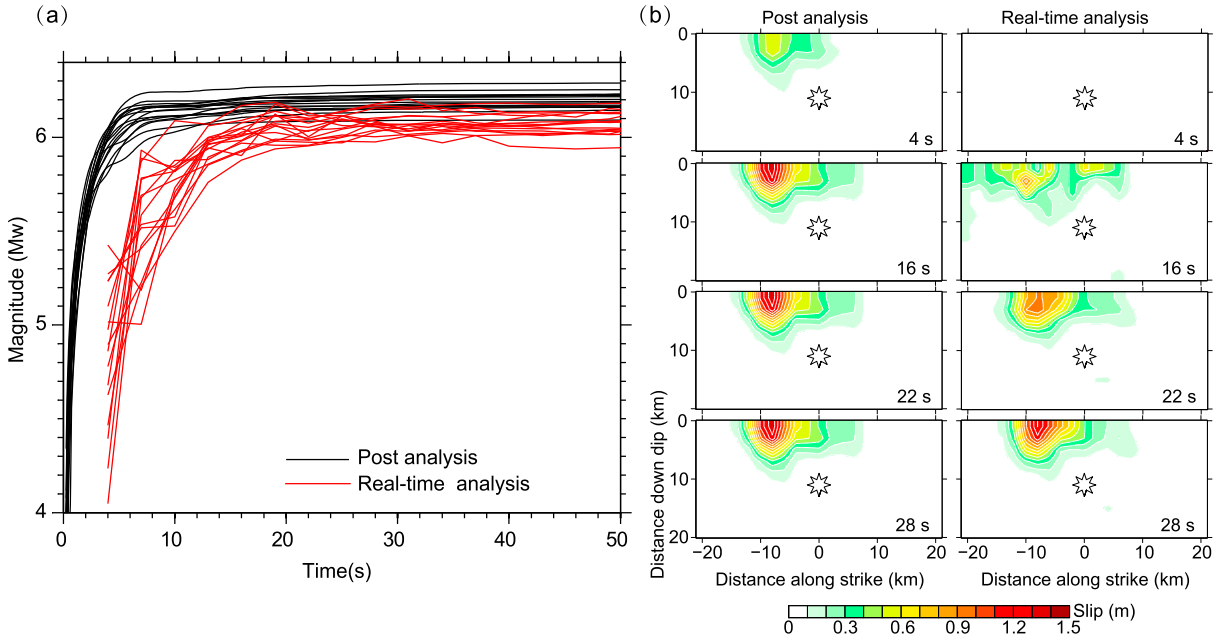

Figure 4. (a) Comparison between the moment magnitudes obtained from the post and real-time analyses for the 16 cases shown in Figure 3. (b) Comparison between the time-dependent fault slips from the post and real-time analyses (only for the case shown in the upper left subgraph in Figure 3).

seismic waves (mainly *S* waves) from the fault to the various stations. Most magnitudes of real-time analysis reached M_w6.0 at about 13 s after the earthquake origin time and thereafter stabilized at M_w5.9–6.1. Compared to the magnitudes, the fault slips stabilized relatively later. The slip distribution was initially scattered. It began to stabilize (became similar with those of postanalysis in fault dimension and rupture area) at about 16 s and well match the slip models of postanalysis at 22–28 s. Compared with the magnitude stabilization, slip stabilized relatively later (Figure 4b). This is because at the beginning the near-fault stations record more source energy than the off-fault stations, causing the waveform information at different stations to lack coherence with each other. By inverting these incoherent waves, seismic moments can be partly estimated, but the positions of fault slips are less constrained.

6. Discussion and Conclusions

By testing different networks, epicenters, and fault geometries, we have demonstrated that the key source parameters of the 2014 South Napa earthquake can be stably determined through automatic source imaging. The magnitude stabilizes at about M_w6.1, with an uncertainty of ±0.1. Slip distributions (Figures 2 and 3) retrieved from these tests consistently show that the rupture unilaterally propagated to the north and at shallow depths. The peak slips are stably estimated in most cases but show a relatively large uncertainty if some reasonable errors of epicenter and fault geometry were considered. Through the real-time analysis, the magnitude reaches M_w6.0 at 13 s after the rupture initiation, while the slip distribution began to stabilize at 16 s.

An important issue needed to be discussed is that we did not determine the source mechanism or fault geometry. As many moderate to large earthquakes occur on preexisting faults, the fault geometry could be well known once the hypocenter was determined in most cases. Thus, in some studies of fault slip investigations, the fault geometry was supposed to be known in advance [*Grapenthin et al.*, 2014]. On the other side, many studies have focused on rapid or real-time determinations of fault geometry and have achieved significant progresses. These studies can be classified into seismic and geodetic inversions. With regional broadband data, *Kawakatsu* [1998] developed a Grid MT method to determine the mechanism in real time. The method was then applied to earthquakes in Japan for fast and routine source analysis [*Tsuruoka et al.*, 2009]. By introducing quasi-finite-source Green's functions into mechanism inversions, *Guilhem and Dreger* [2011] further improved Kawakatsu's method and expanded the scope of application. Recently, *J. Zhang et al.* [2014] speeded up the

mechanism determination by using a search engine method, which reduced the calculation time to less than 1 s. In geodetic studies for large and shallow events, *Melgar et al.* [2012] and *Minson et al.* [2014] inverted smoothed high-rate GPS displacements and suggested that mechanism could be determined earlier than waveform inversions. All of these researches may provide the fault geometry needed in kinematic source imaging.

In this study, we use strong motion seismograms, instead of high-rate GPS time series, to estimate the rupture processes. In principle, high-rate GPS data can be also used for these estimates, which have been demonstrated by many studies [e.g., *Y. Zhang et al.*, 2014]. Compared with strong motion data, high-rate GPS data are more reliable and useful at low frequencies; meanwhile, they are generally noisier at high frequencies. For large earthquakes which induce significant low-frequency signals, high-rate GPS data are undoubtedly a better choice for estimating the source. For moderate earthquakes such as the South Napa quake, because the major frequency band is relatively high, strong motion data would be more appropriate for waveform inversions. Additionally, because of the lower cost, acceleration seismometers are more widely deployed than high-rate GPS receivers. For example, in the epicentral region of the South Napa earthquake, the strong motion network is much denser than the high-rate GPS network. This may be why the magnitude estimated from high-rate GPS data reaches M_w6.0 at 40 s [*Melgar et al.*, 2015], and we found an M_w5.9–6.0 event at about 13 s.

The 2014 South Napa M_w6.1 earthquake is nearly at the lower margin of disastrous earthquakes. Because of the small scale, the seismograms tend to be noisy even at local distances. With strong motion recordings, we have demonstrated that the rupture behaviors of such earthquake can still be robustly and reliably imaged under current observation conditions. In addition to the hypocentral location, focal mechanism, and static fault slip model, a rapid and automatically estimated rupture model would provide other effective source information for fast response of earthquake disasters.

Acknowledgments
The strong motion data of the 2014 South Napa earthquake are from Center for Engineering Strong Motion Data (CESMD). This work is funded by the National Natural Science Foundation of China (NSFC) (41574035, 41541035, and 41090291) and the REAKT project (Towards Real-Time Earthquake Risk Reduction) of the European Seventh Framework Programme (grant agreement 282862).

References

Allen, M. R., P. Gasparini, O. Kamigaichi, and M. Bose (2009), The status of earthquake early warning around the world: An introductory overview, *Seismol. Res. Lett.*, *80*(5), 682–693, doi:10.1785/gssrl.80.5.682.

Allen, R. M., and H. Kanamori (2003), The potential for earthquake early warning in southern California, *Science*, *300*(5620), 786–789.

Allen, R. M., and A. Ziv (2011), Application of real-time GPS to earthquake early warning, *Geophys. Res. Lett.*, *38*, L16310, doi:10.1029/2011GL047947.

Asano, K., and T. Iwata (2009), Source rupture process of the 2004 Chuetsu, Mid-Niigata prefecture, Japan, earthquake inferred from waveform inversion with dense strong-motion data, *Bull. Seismol. Soc. Am.*, *99*(1), 123–140.

Barnhart, W. D., J. R. Murray, S. H. Yun, J. L. Svarc, S. V. Samsonov, E. J. Fielding, and P. Milillo (2015), Geodetic constraints on the 2014 M 6.0 South Napa earthquake, *Seismol. Res. Lett.*, *86*(2A), 335–343.

Beresnev, I. A. (2003), Uncertainties in finite-fault slip inversions: To what extent to believe? (a critical review), *Bull. Seismol. Soc. Am.*, *93*(6), 2445–2458.

Chen, Y., and L. Xu (2000), A time-domain inversion technique for the tempo-spatial distribution of slip on a finite fault plane with applications to recent large earthquakes in the Tibetan Plateau, *Geophys. J. Int.*, *143*, 407–416.

Colombelli, S., R. M. Allen, and A. Zollo (2013), Application of real-time GPS to earthquake early warning in subduction and strike-slip environments, *J. Geophys. Res. Solid Earth*, *118*, 3448–3461, doi:10.1002/jgrb.50242.

Crowell, B. W., Y. Bock, and M. B. Squibb (2009), Demonstration of earthquake early warning using total displacement waveforms from real-time GPS networks, *Seismol. Res. Lett.*, *80*(5), 772–782.

Cua, G., M. Fischer, T. Heaton, and S. Wiemer (2009), Real-time performance of the Virtual Seismologist earthquake early warning algorithm in southern California, *Seismol. Res. Lett.*, *80*(5), 740–747.

Das, S., and B. V. Kostrov (1994), Diversity of solutions of the problem of earthquake faulting inversion: Application to SH waves for the great 1989 Macquarie Ridge earthquake, *Phys. Earth Planet. Inter.*, *85*(3), 293–318.

Dreger, D., and A. Kaverina (2000), Seismic remote sensing for the earthquake source process and near-source strong shaking: A case study of the October 16, 1999 Hector Mine earthquake, *Geophys. Res. Lett.*, *27*, 1941–1944, doi:10.1029/1999GL011245.

Dreger, D. S., L. Gee, P. Lombard, M. H. Murray, and B. Romanowicz (2005), Rapid finite-source analysis and near-fault strong ground motions: Application to the 2003 M_w 6.5 San Simeon and 2004 M_w 6.0 Parkfield earthquakes, *Seismol. Res. Lett.*, *76*(1), 40–48.

Dreger, D. S., M. H. Huang, A. Rodgers, and K. Wooddell (2015), Kinematic finite-source model for the 24 August 2014 South Napa, California, earthquake from joint inversion of seismic, GPS, and InSAR data, *Seismol. Res. Lett.*, *86*(2A), 327–334.

Falck, C., M. Ramatschi, C. Subarya, M. Bartsch, A. Merx, J. Hoeberechts, and G. Schmidt (2010), Near real-time GPS applications for tsunami early warning systems, *Nat. Hazards Earth Syst. Sci.*, *10*(2), 181–189.

Feng, G., Z. Li, X. Shan, B. Xu, and Y. Du (2015), Source parameters of the 2014 Mw6.1 South Napa earthquake estimated from the Sentinel 1A, COSMO-SkyMed and GPS data, *Tectonophysics*, *655*, 139–146.

Grapenthin, R., I. Johanson, and R. M. Allen (2014), The 2014 M_w 6.0 Napa earthquake, California: Observations from real-time GPS-enhanced earthquake early warning, *Geophys. Res. Lett.*, *41*, 8269–8276, doi:10.1002/2014GL061923.

Guilhem, A., and D. S. Dreger (2011), Rapid detection and characterization of large earthquakes using quasi-finite-source Green's functions in continuous moment tensor inversion, *Geophys. Res. Lett.*, *38*, L13318, doi:10.1029/2011GL047550.

Gusman, A. R., Y. Tanioka, B. T. MacInnes, and H. Tsushima (2014), A methodology for near-field tsunami inundation forecasting: Application to the 2011 Tohoku tsunami, *J. Geophys. Res. Solid Earth*, *119*, 8186–8206, doi:10.1002/2014JB010958.

Hartzell, S., P. Liu, C. Mendoza, C. Ji, and K. M. Larson (2007), Stability and uncertainty of finite-fault slip inversions: Application to the 2004 Parkfield, California, earthquake, *Bull. Seismol. Soc. Am.*, *97*(6), 1911–1934.

Hartzell, S. H., and T. H. Heaton (1983), Inversion of strong ground motion and teleseismic waveform data for the fault rupture history of the 1979 Imperial Valley, California, earthquake, *Bull. Seismol. Soc. Am.*, *73*, 1553–1583.

Hayes, G. P., L. Rivera, and H. Kanamori (2009), Source inversion of the W-Phase: Real-time implementation and extension to low magnitudes, *Seismol. Res. Lett.*, *80*(5), 817–822.

Helffrich, G. R. (1997), How good are routinely determined focal mechanisms? Empirical statistics based on a comparison of Harvard, USGS and ERI moment tensors, *Geophys. J. Int.*, *131*(3), 741–750.

Hoechner, A., M. Ge, A. Y. Babeyko, and S. V. Sobolev (2013), Instant tsunami early warning based on real-time GPS—Tohoku 2011 case study, *Nat. Hazards Earth Syst. Sci.*, *12*, 1285–1292, doi:10.5194/nhess-12-1285-2013.

Iida, M., T. Miyatake, and K. Shimazaki (1990), Relationship between strong motion array parameters and the accuracy of source inversion and physical waves, *Bull. Seismol. Soc. Am.*, *80*(6A), 1533–1552.

Ji, C., D. J. Wald, and D. V. Helmberger (2002), Source description of the 1999 Hector Mine, California, earthquake. Part I: Wavelet domain inversion theory and resolution analysis, *Bull. Seismol. Soc. Am.*, *92*, 1192–1207.

Ji, C., R. J. Archuleta, and C. Twardzik (2015), Rupture history of 2014 M_w 6.0 South Napa earthquake inferred from near-fault strong motion data and its impact to the practice of ground strong motion prediction, *Geophys. Res. Lett.*, *42*, 2149–2156, doi:10.1002/2015GL063335.

Kanamori, H., E. Hauksson, and T. Heaton (1997), Real-time seismology and earthquake hazard mitigation, *Nature*, *390*(6659), 461–464.

Kawakatsu, H. (1998), On the realtime monitoring of the long-period seismic wavefield, *Bull. Earthquake Res. Inst. Univ. Tokyo*, *73*, 267–274.

Kikuchi, M., and H. Kanamori (1982), Inversion of complex body waves, *Bull. Seismol. Soc. Am.*, *72*, 491–506.

Li, X., M. Ge, Y. Zhang, B. Guo, R. Wang, J. Klotz, and J. Wicket (2013), Real-time high-rate co-seismic displacement from ambiguity-fixed precise point positioning: Application to earthquake early warning, *Geophys. Res. Lett.*, *40*, 295–300, doi:10.1002/GRL.50138.

Melgar, D., Y. Bock, and B. W. Crowell (2012), Real-time centroid moment tensor determination for large earthquakes from local and regional displacement records, *Geophys. J. Int.*, *188*(2), 703–718.

Melgar, D., J. Geng, B. W. Crowell, J. S. Haase, Y. Bock, W. C. Hammond, and R. M. Allen (2015), Seismogeodesy of the 2014 M_w6.1 Napa earthquake, California: Rapid response and modeling of fast rupture on a dipping strike-slip fault, *J. Geophys. Res. Solid Earth*, *120*, 5013–5033, doi:10.1002/2015JB011921.

Minson, S. E., J. R. Murray, J. O. Langbein, and J. S. Gomberg (2014), Real-time inversions for finite fault slip models and rupture geometry based on high-rate GPS data, *J. Geophys. Res. Solid Earth*, *119*, 3201–3231, doi:10.1002/2013JB010622.

Miyatake, T., M. Iida, and K. Shimazaki (1986), The effect of strong-motion array configuration on source inversion, *Bull. Seismol. Soc. Am.*, *76*(5), 1173–1185.

Monelli, D., and P. M. Mai (2008), Bayesian inference of kinematic earthquake rupture parameters through fitting of strong motion data, *Geophys. J. Int.*, *173*(1), 220–232.

Mori, J., and S. Hartzell (1990), Source inversion of the 1988 Upland, California, earthquake: Determination of a fault plane for a small event, *Bull. Seismol. Soc. Am.*, *80*(3), 507–518.

Okada, Y. (1985), Surface deformation due to shear and tensile faults in a half-space, *Bull. Seismol. Soc. Am.*, *75*(4), 1135–1154.

Olson, A. H., and J. G. Anderson (1988), Implications of frequency-domain inversion of earthquake ground motions for resolving the space-time dependence of slip on an extended fault, *Geophys. J. Int.*, *94*(3), 443–455.

Olson, A. H., and R. J. Apsel (1982), Finite faults and inverse theory with applications to the 1979 Imperial Valley earthquake, *Bull. Seismol. Soc. Am.*, *72*, 1969–2001.

Pollitz, F. F., R. Bürgmann, and P. Banerjee (2011), Geodetic slip model of the 2011 M9.0 Tohoku earthquake, *Geophys. Res. Lett.*, *38*, L00G08, doi:10.1029/2011GL048632.

Sarao, A., S. Das, and P. Suhadolc (1998), Effect of non-uniform station coverage on the inversion for earthquake rupture history for a Haskell-type source model, *J. Seismol.*, *2*(1), 1–25.

Stidham, C., M. Antolik, D. Dreger, S. Larsen, and B. Romanowicz (1999), Three-dimensional structure influences on the strong motion wavefield of the 1989 Loma Prieta earthquake, *Bull. Seismol. Soc. Am.*, *89*, 1184–1202.

Tsuruoka, H., H. Kawakatsu, and T. Urabe (2009), GRiD MT (grid-based real-time determination of moment tensors) monitoring the long-period seismic wavefield, *Phys. Earth Planet. Inter.*, *175*, 8–16, doi:10.1016/j.pepi.2008.02.014.

Vallée, M. (2004), Stabilizing the empirical Green's function analysis: Development of the projected Landweber method, *Bull. Seismol. Soc. Am.*, *94*, 394–409.

Wald, D. J., D. V. Helmberger, and T. H. Heaton (1991), Rupture model of the 1989 Loma Prieta earthquake from the inversion of strong-motion and broadband teleseismic data, *Bull. Seismol. Soc. Am.*, *81*(5), 1540–1572.

Wang, R. (1999), A simple orthonormalization method for stable and efficient computation of Green's functions, *Bull. Seismol. Soc. Am.*, *89*(3), 733–7410.

Wang, R., F. Lorenzo-Martín, and F. Roth (2006), PSGRN/PSCMP—A new code for calculating co-and post-seismic deformation, geoid and gravity changes based on the viscoelastic-gravitational dislocation theory, *C. R. Geosci.*, *32*(4), 527–541.

Wang, R., S. Parolai, M. Ge, M. Jin, T. R. Walter, and J. Zschau (2013), The 2011 M_w 9.0 Tohoku earthquake: Comparison of GPS and strong-motion data, *Bull. Seismol. Soc. Am.*, *103*(2B), doi:10.1785/0120110264.

Wei, S., S. Barbot, R. Graves, J. J. Lienkaemper, T. Wang, K. Hudnut, and D. Helmberger (2015), The 2014 M_w 6.1 South Napa earthquake: A unilateral rupture with shallow asperity and rapid afterslip, *Seismol. Res. Lett.*, *86*(2A), 344–354.

Wright, T. J., N. Houlie, M. Hildyard, and T. Iwabuchi (2012), Real-time, reliable magnitudes for large earthquakes from 1 Hz GPS precise point positioning: The 2011 Tohoku-Oki (Japan) earthquake, *Geophys. Res. Lett.*, *39*, L12302, doi:10.1029/2012GL051894.

Wurman, G., R. M. Allen, and P. Lombard (2007), Toward earthquake early warning in northern California, *J. Geophys. Res.*, *112*, B08311, doi:10.1029/2006JB004830.

Yagi, Y., T. Mikumo, J. Pacheco, and G. Reyes (2004), Source rupture process of the Tecomán, Colima, Mexico earthquake of 22 January 2003, determined by joint inversion of teleseismic body-wave and near-source data, *Bull. Seismol. Soc. Am.*, *94*, 1795–1807.

Zhang, J., H. Zhang, W. Chen, Y. Zheng, W. Kuang, and X. Zhang (2014), Real-time earthquake monitoring using a search engine method, *Nat. Commun.*, *5*, doi:10.1038/ncomms6664.

Zhang, Y., W. P. Feng, Y. T. Chen, L. S. Xu, Z. H. Li, and D. Forrest (2012), The 2009 L'Aquila M_w 6.3 earthquake: A new technique to locate the hypocentre in the joint inversion of earthquake rupture process, *Geophys. J. Int.*, *191*, 1417–1426, doi:10.1111/j.1365-246X.2012.05694.x.

Zhang, Y., R. Wang, J. Zschau, Y. Chen, S. Parolai, and T. Dahm (2014), Automatic imaging of earthquake rupture processes by iterative deconvolution and stacking of high-rate GPS and strong-motion seismograms, *J. Geophys. Res. Solid Earth*, *119*, 5633–5650, doi:10.1002/2013JB010469.

Zhang, Y. B., L. A. Dalguer, S. G. Song, and J. Clinton (2015), Evaluating the effect of network density and geometric distribution on kinematic source inversion models, *Geophys. J. Int.*, *200*, 1–16.

Zhou, S., K. Irikura, and X. Chen (2004), Analysis of the reliability and resolution of the earthquake source history inferred from waveforms, taking the Chi-Chi earthquake as an example, *Geophys. J. Int.*, *157*(3), 1217–1232.